


 Cite this: *RSC Adv.*, 2024, **14**, 3659

## Rheological and radioactive decontamination properties of ethyl cellulose sols in green solvents at a temperature below 0 °C†

 Xunhai Pan,<sup>ab</sup> Xiaoyan Lin,<sup>id</sup> \*<sup>ac</sup> Hao Zhang,<sup>a</sup> Lili Liang,<sup>a</sup> Chunxia Pang,<sup>ab</sup> Kai Gu,<sup>a</sup> Yang Hu<sup>a</sup> and Hailing Xi<sup>\*d</sup>

Strippable film decontamination has been considered one of the best prospects for radioactive surface decontamination due to its high decontamination effect and less secondary pollution. However, research into strippable films has until now focused on radioactive decontamination at room temperature. Therefore, it is vital to seek a suitable degradable material for preparing strippable films in removing contaminants in an extremely cold region, as it will face the problem of the freezing of the detergent. Ethyl cellulose (EC) is a kind of degradable biopolymer which is easily dissolved in volatile green organic solvents to form a sol below 0 °C which is advantageous for forming a film. Therefore, it would be the best choice for preparing a strippable film detergent. In this study, EC sols were obtained by placing EC powder into the green solvents anhydrous ethanol and ethyl acetate. The steady and dynamic rheological behavior of EC sols was investigated with a rotary rheometer with the temperature ranging from -10 °C to 0 °C to disclose their spraying performance. Moreover, the radioactive decontamination effect of EC sols and the mechanism were also investigated. The results showed that the EC sols were pseudoplastic fluids which obeyed the Ostwald–de Waele power law below 0 °C. Furthermore, the viscosity of EC sols could be reduced by stirring, which is convenient for large-area spraying during decontamination below 0 °C. At -10 °C, the comprehensive decontamination rates of all plates were over 85%. Therefore, EC sols could be used as a basic material for strippable film decontamination below 0 °C.

Received 29th September 2023

Accepted 9th January 2024

DOI: 10.1039/d3ra06641j

[rsc.li/rsc-advances](http://rsc.li/rsc-advances)

### 1. Introduction

To face the energy crisis, nuclear power, as a stable form of green energy, has been extensively developed for decades.<sup>1</sup> However, nuclear accidents along with radioactive waste pose a great threat to humans and the environment. The Chernobyl and Fukushima nuclear accidents caused serious pollution to the environment around them, which did a great deal of harm to human health.<sup>2–6</sup> The Fukushima nuclear disaster resulted from an inadequate nuclear emergency response.<sup>7</sup> Therefore, it is of great significance to deal with radioactive contamination promptly for the protection of the environment and human society.

At present, there are many surface decontamination technologies, including chemical or physical methods, supercritical fluid methods, electrochemical methods, laser methods, stripping film methods and foam methods.<sup>8–14</sup> Among these methods, the stripping film method is a promising method for decontaminating radioactive pollutants due to its high decontamination rate and less secondary pollution.<sup>15,16</sup> Stripping film decontaminating technologies at room temperature have already been extensively reported and discussed.<sup>17–21</sup> However, there are few reports on stripping film decontamination at temperatures below 0 °C.<sup>16,22</sup> It is urgent to develop a stripping film decontaminating material to be applied below 0 °C because of the poor spraying properties in a low-temperature environment. At the same time, it is very important to minimize the volume of decontaminating film in order to reduce the costs of storage, transportation and disposal after decontamination. The degradation of decontaminating film is one important method to minimize the volume. Therefore, the preparation of decontaminating film should apply a degradable material to minimize the volume. Biomass-based materials, due to their degradable properties, have become the prospective choice for preparing detergents.

Cellulose, as a kind of biodegradable polymer which is renewable and widely available, has aroused great interest from

<sup>a</sup>School of Materials and Chemistry, Southwest University of Science and Technology, 621010 Mianyang, Sichuan, China. E-mail: lxy20100205@163.com

<sup>b</sup>School of Bioengineering, Sichuan University of Science and Engineering, 644005 Yibin, Sichuan, China

<sup>c</sup>Engineering Research Center of Biomass Materials, Ministry of Education, Southwest University of Science and Technology, 621010 Mianyang, Sichuan, China

<sup>d</sup>State Key Laboratory of NBC Protection for Civilian, 102205 Beijing, China. E-mail: fhxihl@163.com

† Electronic supplementary information (ESI) available. See DOI: <https://doi.org/10.1039/d3ra06641j>



researchers.<sup>23</sup> While ethyl cellulose (EC) obtained from the modification of cellulose, which is also degradable, has been widely used in film, textile, food, pharmaceutical, and coating applications.<sup>24–28</sup> Besides, EC could be dissolved in a green organic solvent such as ethyl acetate and so could be volatile and flow at low temperature. Therefore, it has probably become the most preferred basic material in preparing a strippable film. To perform decontamination at low temperature successfully, it is necessary to understand the rheological behavior of EC sols at low temperature. The rheological behavior of cellulose dissolved in ionic liquids (ILs) has been carefully researched.<sup>29–31</sup> The effect of the rheological behavior of inks which contained 6–15 wt% of cellulose nanocrystals (CNC) on 3D-printability has been evaluated.<sup>32</sup> The rheological behavior of some cellulose derivatives has also been studied. For example, the rheological behavior of hydroxypropyl cellulose (HPC) solution and hydroxy ethyl cellulose (HEC) dispersions has been studied.<sup>33,34</sup> The rheological properties of ceramic pastes together with EC dissolved in ethylene glycol monobutyl ether acetate were investigated by K. Inukai *et al.*<sup>35</sup> However, understanding of the properties of EC sols has been rather limited until now, especially in the case of organic solvents at a temperature below 0 °C. Moreover, the decontamination characteristics and rheological properties of EC sols at low temperature have rarely been reported. Therefore, it is very important to know the characteristic of EC sols at a temperature below 0 °C.

In this study, EC sols were prepared by dissolving EC in green volatile organic solvents of anhydrous ethanol and ethyl acetate which had the characteristics of low freezing and rapid volatilization. The spraying properties were analyzed by investigating the rheological behavior of EC sols at a low temperature below 0 °C. The radioactive decontamination efficiencies of EC sols on different kinds of plates at –10 °C were also studied. The results of the rheological behavior and decontamination properties of EC sols revealed that the EC sols have extensive application prospects in strippable film decontamination at low temperatures below 0 °C.

## 2. Materials and methods

### 2.1 Materials

Anhydrous ethanol, ethyl acetate, ChengDu Chron Chemicals Co., Ltd.; ethyl cellulose (intrinsic viscosity 90–110 mPa s; 5% in toluene/isopropanol 80 : 20 (v/v)), Shanghai Aladdin Biochemical Technology Co., Ltd.; uranyl nitrate, Chushengwei Chemical Co., Ltd. All reagents were analytically pure (AR).

Ethyl cellulose (EC) sols were obtained by dissolving a certain amount of EC in a mixed solvent of anhydrous ethanol and ethyl acetate. The EC sols were stirred at room temperature for 12 h in a flask to make the sol homogeneous. The content of anhydrous ethanol in the mixed solvent was 10% (v/v).

### 2.2 Methods

**2.2.1 Rheology analysis.** The rheology behavior of the EC sols was measured with a rotary rheometer (HAAKE MARS II, Thermo Fisher Scientific Ltd.) equipped with a temperature

control system. The shear stress of the EC sols was tested over a range in shear rate from 0.1 to 100 s<sup>–1</sup> and with temperatures of –10 °C and 0 °C. The viscosity of the EC sols was also measured in the temperature range from –10 to 0 °C and with a shear rate of 50 s<sup>–1</sup>. The storage modulus ( $G'$ ) and loss modulus ( $G''$ ) of the EC sols were measured by sweeping in dynamic mode with the frequency ranging from 0.1 to 10 Hz and the temperature ranging from –10 °C to 0 °C.

**2.2.2 Radioactive decontamination study on different kinds of plates.** Uranyl nitrate was used to simulate the contaminated radioactive surface of different plates (10 × 10 cm). The radioactive count rate of the plates was detected with a surface radioactivity monitor (FJ-2207, Xi'an China Nuclear Instrument Co., Ltd.) with the test distance kept at 5 mm. The background radioactive count rate of each plate was measured and recorded as  $L_0$ . The surface of each piece of plate was evenly sprinkled with uranyl nitrate. The count rate of each contaminated plate was measured and recorded as  $L_1$ . At the desired temperature, the EC sols were poured on the different plates and left to stand for 24 h to form films which were peeled off afterwards. After the films were stripped, the radioactive count rate of each plate was tested and denoted as  $L_2$ .

The decontamination rate (DR) was calculated in accordance with eqn (1):

$$DR = \frac{L_1 - L_2}{L_1 - L_0} \times 100\% \quad (1)$$

**2.2.3 Chemical structure and morphological analysis.** In this work, FTIR (Nicolet 5700, Thermo, America) was applied to confirm the structure of the peeled films being recorded in the range from 4000 cm<sup>–1</sup> to 500 cm<sup>–1</sup>. XPS spectra were recorded on an X-ray photoelectron spectrometer (Thermo Scientific K-Alpha, Thermo, America). The micro-morphologies and elemental composition of the EC films were analyzed with a scanning electron microscope (MERLIN Compact, ZEISS, Germany) at an accelerating voltage of 5 kV and energy dispersive spectroscopy (EDS, Oxford X-Max, Oxford, England), respectively.

## 3. Results and discussion

### 3.1 Study of rheological properties with a steady shear rate

It is known that the leveling, sagging and spraying properties of the detergents could be reflected in the rheological properties, which are significantly affected by the polymer concentration and environmental temperature. Furthermore, a favorable detergent applied at low temperature should have good fluidity for easy spraying. Therefore, it is necessary to understand the rheological behavior of EC sols at low temperature to perform decontamination at low temperature successfully. The steady shear rheological properties of the EC sols at a temperature below 0 °C were studied by applying a rotary rheometer, and the rheological curves of the EC sols are shown in Fig. 1.

Fig. 1(a)–(c) show the variation in shear stress ( $\tau$ ) along with shear rate ( $\dot{\gamma}$ ) (0.1–100 s<sup>–1</sup>) for 7 wt% EC sol, 9 wt% EC sol, and 11 wt% EC sol at temperatures of 0 °C and –10 °C, respectively.



It was obvious that the shear stress of the three kinds of EC sol increased with the increase in shear rate, temperature ( $T$ ) and EC concentration. Meanwhile, the shear stress of the EC sol at  $-10\text{ }^{\circ}\text{C}$  was greater than that of the EC sol at  $0\text{ }^{\circ}\text{C}$  under the same shear rate. Contrasting Fig. 1(a)–(c), the relationship between shear stress and shear rate of the sol with 7 wt% EC was close to linear. In contrast, the flow curve of shear stress along with shear rate became more nonlinear with increasing EC concentration. Accordingly, the slope of the shear stress *versus* shear rate ( $\tau \sim \dot{\gamma}$ ) curve decreased with increasing shear rate, which indicated that the EC sols showed shear rate dependency,<sup>36</sup> and the EC sols showed shear thinning characteristics. This confirmed that the EC sol is a pseudoplastic fluid, a kind of non-Newtonian fluid. Additionally, the viscosity of the EC sols could be reduced by stirring, which was convenient for large-area spraying during decontamination at a temperature below  $0\text{ }^{\circ}\text{C}$ .

Regression analysis was conducted on the relevant experimental data using the Ostwald–de Waele power law,<sup>37</sup> as shown in eqn (2):

$$\tau = k\dot{\gamma}^n \quad (2)$$

where  $\tau$  is the shear stress,  $k$  is the consistency index,  $\dot{\gamma}$  is the shear rate and  $n$  is the flow behavior index.

The parameters shown in Table 1, calculated according to eqn (2), show that the rheological properties of the EC sols were classical shear thinning behavior. Besides, the relationship between the shear stress ( $\tau$ ) and the shear rate ( $\dot{\gamma}$ ) could fit well with the Ostwald–de Waele power law.

The greater the viscosity of the sol, the greater the viscosity coefficient ( $k$ ). As shown in Table 1, the viscosity coefficient ( $k$ ) of the sol with 7 wt% EC decreased from 2.5309 at  $-10\text{ }^{\circ}\text{C}$  to 1.4409 at  $0\text{ }^{\circ}\text{C}$ , and the viscosity coefficient ( $k$ ) of the sol with 9 wt% EC decreased from 6.6625 at  $-10\text{ }^{\circ}\text{C}$  to 1.2405 at  $0\text{ }^{\circ}\text{C}$ . The

Table 1 Rheological parameters of EC sols

Sample	Conc. (wt%)	Temperature (°C)	Rheological parameters		
			$k$	$n$	$R^2$
EC sols	7	-10	2.5309	0.9504	0.9992
		0	1.4409	0.9778	0.9999
	9	-10	6.6625	0.9137	0.9958
		0	1.2405	0.9864	0.9997
	11	-10	16.9060	0.8660	0.9890
		0	9.9940	0.8858	0.9970

viscosity coefficient ( $k$ ) of the sol with 11 wt% EC decreased from 16.9060 at  $-10\text{ }^{\circ}\text{C}$  to 9.9940 at  $0\text{ }^{\circ}\text{C}$ , which indicated that the viscosity of the EC sols decreased as the temperature increased and the concentration of EC decreased.

The smaller the flow behavior index ( $n$ ), the stronger the non-Newtonian property of the sol. Table 1 shows that the  $n$  values of the sol with 7 wt% EC at  $-10\text{ }^{\circ}\text{C}$  and  $0\text{ }^{\circ}\text{C}$  were greater than 0.9504, that is, close to 1. Moreover, the  $n$  of the sol with 7 wt% EC was not obviously changed with temperature, and the non-Newtonian property of the sol with 7 wt% EC was low. The reason could be that the probability of overlapping and entangling between EC polymer chains was less in a dilute solution.

As shown in Table 1, the  $n$  values of the sol with 9 wt% EC were greater than those of the sol with 11 wt% EC at  $-10\text{ }^{\circ}\text{C}$  and  $0\text{ }^{\circ}\text{C}$ , respectively. The  $n$  of the sol decreased, and the non-Newtonian property increased with increasing EC concentration. The  $n$  values of the sols with 9 wt% EC and 11 wt% EC increased with increasing temperature. The thermal motion of the molecular chain segments accelerated, and the intermolecular force decreased with increasing temperature. The viscosity of the EC sols decreased as the temperature increased, and the EC sols showed less non-Newtonian properties but more Newtonian properties.

Fig. 1(d) shows the viscosity changes in EC sols with the temperature ranging from  $-10\text{ }^{\circ}\text{C}$  to  $0\text{ }^{\circ}\text{C}$ . The viscosity of 7 wt% EC sol increased from  $1.1766\text{ Pa s}$  to  $2.0400\text{ Pa s}$  when the temperature was reduced from  $0\text{ }^{\circ}\text{C}$  to  $-10\text{ }^{\circ}\text{C}$ . In comparison, the viscosity of the sol with 9 wt% EC increased from  $2.9110\text{ Pa s}$  to  $5.4310\text{ Pa s}$  when the temperature was reduced within the same testing range, while the sol viscosity of 11 wt% EC increased from  $6.5566\text{ Pa s}$  to  $11.4700\text{ Pa s}$ . This could be explained by the molecular chain moving more slowly at the lower temperature together with shrinkage of the polymer chains, resulting in tight winding and overlapping between polymer chains and the enhancing of intermolecular interaction, finally leading to increasing viscosity with decreasing temperature. In contrast, the molecular thermodynamic movement in the sol quickened with increasing temperature, and the interaction between the polymer chains of EC was weakened, which led to the loose winding of the polymer chains and finally to the decrease in viscosity. Fig. 1(d) also shows that the viscosity of EC sols increased with increasing EC concentration at the same temperature. The reason could be that the probability of overlapping and entangling between EC polymer chains

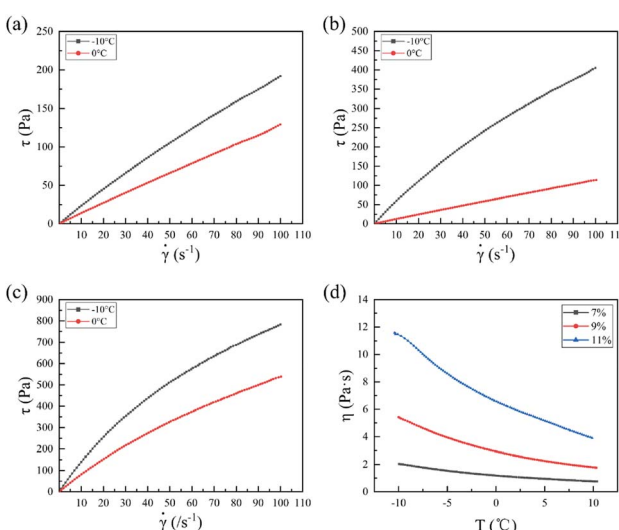


Fig. 1 Variation of shear stress ( $\tau$ ) along with shear rate ( $\dot{\gamma}$ ) for (a) 7 wt% EC sol, (b) 9 wt% EC sol, (c) 11 wt% EC sol. (d) The viscosity ( $\eta$ ) changes of the EC sols with change in temperature.



increased with increasing EC concentration, and the interaction between polymer chains increased.

### 3.2 Dynamic oscillation rheological behavior of EC sols

The storage modulus ( $G'$ ) and loss modulus ( $G''$ ) of the EC sols with changes in frequency at temperatures of  $-10\text{ }^{\circ}\text{C}$  and  $0\text{ }^{\circ}\text{C}$  are shown in Fig. 2.

It was obvious that the  $G'$  and  $G''$  of the three kinds of EC sols increased with increasing frequency. The  $G'$  and  $G''$  increased more quickly when the frequency was low, and increased more slowly at higher frequency. At the same frequency, the  $G'$  and  $G''$  of the EC sols always decreased in the order of 11 wt% EC, 9 wt% EC, 7 wt% EC, at temperatures of  $0\text{ }^{\circ}\text{C}$  and  $-10\text{ }^{\circ}\text{C}$ . At the temperature of  $0\text{ }^{\circ}\text{C}$ , with the decrease in EC concentration from 11 wt% to 7 wt%, the  $G'$  of the EC sol decreased from 320.80 Pa to 17.50 Pa, and the  $G''$  of the EC sol decreased from 598.80 Pa to 85.81 Pa at the frequency of 10 Hz. At the temperature of  $-10\text{ }^{\circ}\text{C}$ , with the decrease in EC concentration from 11 wt% to 7 wt%, the  $G'$  of the EC sol decreased from 346.70 Pa to 27.41 Pa, and the  $G''$  of the EC sol decreased from 774.50 Pa to 134.20 Pa at the frequency of 10 Hz.

Fig. 3 shows the complex viscosity ( $|\eta^*|$ ) for the EC sols with changing frequency at  $0\text{ }^{\circ}\text{C}$  and  $-10\text{ }^{\circ}\text{C}$ .

At the same frequency, the complex viscosity of the EC sols always decreased in the order of 11 wt% EC, 9 wt% EC, 7 wt% EC, at temperatures of  $0\text{ }^{\circ}\text{C}$  and  $-10\text{ }^{\circ}\text{C}$ . The complex viscosity for the samples showed a plateau while the frequencies were low, which indicated that chain entanglement occurred.<sup>38</sup> The complex viscosity ( $|\eta^*|$ ) increased with increasing concentration of EC, because the higher concentration of EC produced many entanglements in the sols. At higher frequency, the complex viscosity of the EC sols decreased little with further increase in the frequency. The complex viscosity of EC sols showed a constant value at higher frequencies below  $0\text{ }^{\circ}\text{C}$ .

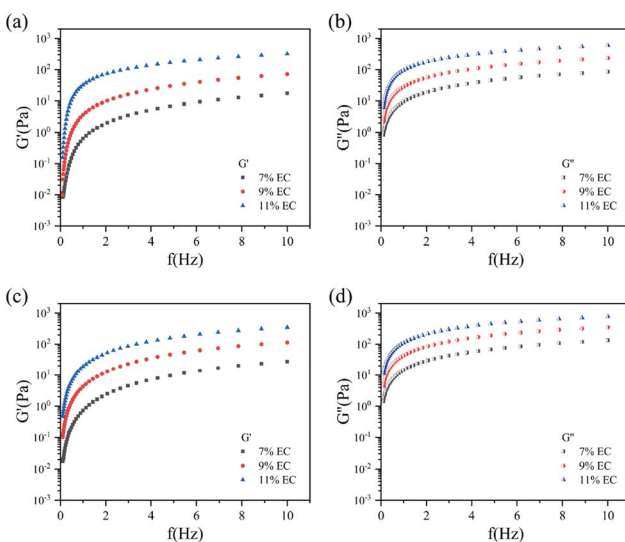


Fig. 2 Storage modulus ( $G'$ ) and loss modulus ( $G''$ ) for the EC sols with changing frequency ( $f$ ) at temperatures of (a) and (b)  $0\text{ }^{\circ}\text{C}$  and (c) and (d)  $-10\text{ }^{\circ}\text{C}$ , respectively.

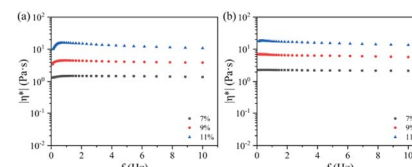


Fig. 3 Complex viscosity ( $|\eta^*|$ ) of the EC sols with changing frequency at (a)  $0\text{ }^{\circ}\text{C}$ , (b)  $-10\text{ }^{\circ}\text{C}$ .

Fig. 4 shows the  $G'$  and  $G''$  of the EC sols with 7 wt%, 9 wt%, and 11 wt% EC as a function of temperature ranging from  $-10\text{ }^{\circ}\text{C}$  to  $0\text{ }^{\circ}\text{C}$ .

As shown in Fig. 4, the  $G'$  of the sols with 7 wt%, 9 wt%, and 11 wt% EC were almost all less than their  $G''$  when the temperature ranged from  $-10$  to  $0\text{ }^{\circ}\text{C}$ . The result showed that the EC sols mainly exhibited viscous behavior and they could flow and be favorable for spraying above  $-10\text{ }^{\circ}\text{C}$ .

### 3.3 Radioactive decontamination by EC sols and its mechanism

**3.3.1 Radioactive decontamination properties.** The EC could be applied as a film-forming material because can easily form a film.<sup>39</sup>

The film-forming properties of EC sols were studied by pouring the EC sols over the surfaces of marble, ceramic tile, glass, stainless steel and concrete to be dried and form films at  $-10\text{ }^{\circ}\text{C}$ ,  $0\text{ }^{\circ}\text{C}$  and room temperature, respectively. The film-forming properties were observed and recorded every two hours. The results showed that the film-forming time of the EC sols was shorter with higher drying temperature. The film-forming time of the EC sols was about 4 hours at room temperature and about 22 hours at  $-10\text{ }^{\circ}\text{C}$ . To ensure that the EC sols are completely dry at  $-10\text{ }^{\circ}\text{C}$ , 24 h was chosen for the drying time of the EC sols. Fig. S1† shows photographic images of the EC films after the EC sols had been dried for 24 h. After the EC sols had been dried, the EC films are almost self-peeling off the surface of marble, ceramic tile, glass and stainless steel, and are very easy to peel off. The EC film cannot be self-peeled off the concrete surface, but it can be peeled off completely.

Fig. 5 shows the changes in the decontamination rate of the 9 wt% EC sol on different plates as a function of spraying dose at  $-10\text{ }^{\circ}\text{C}$ . As shown in Fig. 5, the  $\alpha$  decontamination rates ( $\alpha$  DR) on marble, ceramic tile, glass, and stainless steel changed little with spraying dose in the range of 7–13 mL/100 cm<sup>2</sup>. While the  $\alpha$  DR on concrete shows a great change with spraying dose. The  $\beta$  decontamination rate ( $\beta$  DR) on the above five plates shows a great change with the spraying dose in the range of 7–13 mL/100 cm<sup>2</sup>. Considering the decontamination rate and economy, the optimal spraying dose of the EC sols is 10 mL/100 cm<sup>2</sup>.

The decontaminating properties of EC sols at  $-10\text{ }^{\circ}\text{C}$  for radioactive contaminants on different plates were investigated with the dose of EC sols being 10 mL/100 cm<sup>2</sup>. The decontamination rates of the EC sols are shown in Fig. 6.



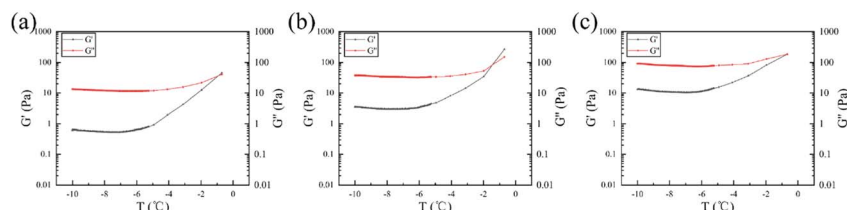


Fig. 4  $G'$  and  $G''$  of the EC sols with changing temperature: (a) 7 wt% EC sol. (b) 9 wt% EC sol. (c) 11 wt% EC sol.

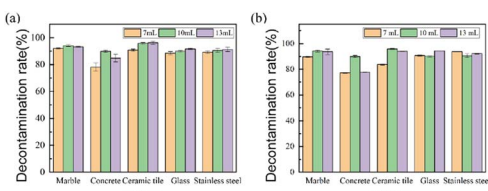


Fig. 5 Changes in the decontamination rate of 9 wt% EC sol as a function of spraying dose on different plates at  $-10\text{ }^{\circ}\text{C}$ : (a)  $\alpha$  DR, (b)  $\beta$  DR.

Fig. 6(a) shows that the  $\alpha$  DR and  $\beta$  DR of the 7 wt% EC sol on the concrete plate at  $-10\text{ }^{\circ}\text{C}$  were 85.80% and 89.19%, respectively. The  $\alpha$  DR and  $\beta$  DR on the other plates were all over 90.00%. The comprehensive decontamination rates on different plates for the 7 wt% EC sol decreased according to the following rules: ceramic tile > marble > glass > stainless steel > concrete. In contrast, the  $\alpha$  DR and  $\beta$  DR on the concrete plate were 84.30% and 89.84%, respectively, as shown in Fig. 6(b) when the EC sol was 9 wt%. Additionally, the  $\beta$  DR on the glass plate was 89.97% while they were all over 90% on the other three plates. The comprehensive decontamination rate on different plates for the 9 wt% EC sol decreased according to the following rules: ceramic tile > marble > stainless steel > glass > concrete. Fig. 6(c) shows that, at  $-10\text{ }^{\circ}\text{C}$ , the  $\alpha$  DR of the 11 wt% EC sol on the concrete plate was only 85.23%, and the  $\beta$  DR on the stainless steel plate was 89.87%, while the other values were all over 90%. The comprehensive decontamination rate on different plates for the 11 wt% EC sol decreased according to the following rules: ceramic tile > glass > marble > stainless steel > concrete. When the concentration of EC in the sol rises from 7 to 11 wt%, the  $\alpha$  DR and  $\beta$  DR of the EC sols on all five different kinds of surface changed little. Moreover, the comprehensive

decontamination rate on concrete was over 85% while it was over 90% on the other four kinds of plate.

Fig. S2† shows the decontamination rates of the EC sols at room temperature. Obviously, the decontaminating properties of EC sols at room temperature are below those at a temperature below  $0\text{ }^{\circ}\text{C}$ .

### 3.3.2 Mechanism analysis.

Fig. 7 shows the FTIR spectra of the EC films before and after decontamination.

As depicted in Fig. 7, the adsorption peak at  $3479\text{ cm}^{-1}$  was assigned to O-H stretching vibration in the EC chains,<sup>40,41</sup> and the adsorption peaks at  $2973\text{ cm}^{-1}$  and  $2877\text{ cm}^{-1}$  were attributed to the stretching vibration of methyl and methylene groups.<sup>25</sup> The adsorption peak at  $1376\text{ cm}^{-1}$  was related to the C-H bending vibration.<sup>42</sup> The broad absorption band at  $1110\text{ cm}^{-1}$  was associated with the C-O stretching vibration.<sup>43,44</sup> In comparison, the adsorption peaks of the EC films after decontamination, shown in Fig. 7 at  $3479\text{ cm}^{-1}$ ,  $2973\text{ cm}^{-1}$ ,  $2877\text{ cm}^{-1}$ ,  $1376\text{ cm}^{-1}$  and  $1110\text{ cm}^{-1}$ , changed little, which confirmed the stability of the EC films.

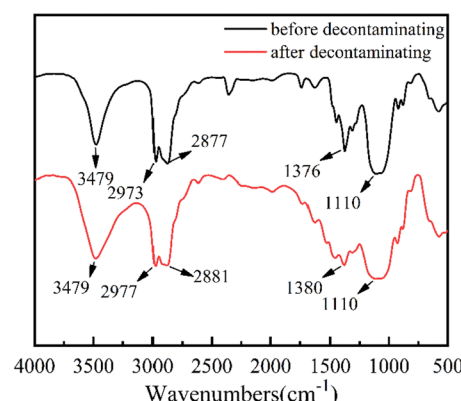


Fig. 7 A comparison of the FTIR spectra of EC films.

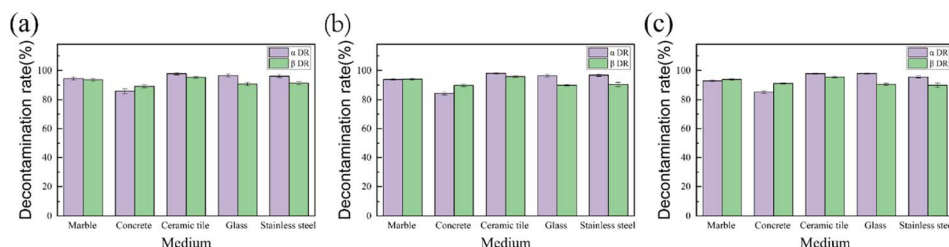


Fig. 6 Decontamination rate on different plates at  $-10\text{ }^{\circ}\text{C}$ : (a) 7 wt% EC sol, (b) 9 wt% EC sol, (c) 11 wt% EC sol.



The changes in the morphological structure of the EC films were investigated by comparing the SEM images of the EC films before and after decontamination, as shown in Fig. 8.

As demonstrated in Fig. 8(a), the SEM images indicate that the surface of the EC film before decontamination is smooth and there were some small pores distributed uniformly in the film, which was advantageous for the contaminants being enveloped and fixed on the EC film. However, the pores became fewer, and many uniform craters appeared in the film after decontamination (Fig. 8(b) and (c)). One reason might be that uranyl ions were complexed with O-H in the EC polymer chains, and an EC-U complex, centered on the uranyl ion, was formed between multiple EC polymer chains. So, the distance between different EC polymer chains became narrow, and the EC polymer chains further interacted to form a uniform and fine network structure. The elemental mapping images (Fig. 8(d)–(g)) and energy dispersive spectroscopy (Fig. 8(h)) demonstrate that the elements of the EC film after decontamination are C, O, N, and U. The simulated uranium contamination is dispersed into the EC film.

Fig. 9 shows X-ray photoelectron spectroscopy (XPS) analysis of the EC film after decontamination.

The overall spectrum (Fig. 9(a)) shows the main constituent elements of the EC film after decontamination, where the peaks around 285, 383 and 533 were C, U and O, respectively. As for the C 1s spectrum (Fig. 9(b)), the peaks at 284.8 eV, 286.6 eV and 289.0 eV represent C-C, C-O and C=O.<sup>45</sup> Fig. 9(c) shows the peak fitting diagram for O 1s, in which the O 1s spectrum was

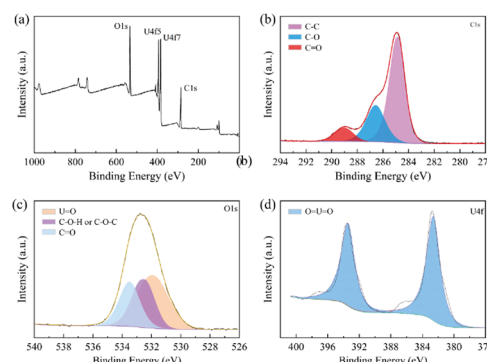


Fig. 9 XPS spectra of EC film after decontamination: (a) full spectrum; (b) C 1s spectrum; (c) O 1s spectrum; (d) U 4f spectrum.

divided into three main peaks at 531.9 eV, 532.5 eV and 533.5 eV corresponding to U=O, C-O-H or C-O-C, and C=O, respectively. Fig. 9(d) shows the double peak of U 4f of  $\text{UO}_2^{2+}$  at 382.7 eV and 393.5 eV.<sup>41</sup> Therefore, the XPS results illustrate that the simulated uranium contamination is in the EC films.

The decontamination mechanism of the EC sols was disclosed by comprehensive analysis of FTIR, SEM-EDS, XPS and decontamination efficiency results. The probable decontamination mechanism is illustrated in Fig. 10.

During the decontamination process, an EC sol layer formed after the sols had flowed and coated the different surfaces of the contaminants.<sup>16</sup> As shown in Fig. 10, the uranyl nitrate would be wrapped and gradually dissolved into anhydrous ethanol in the sols and be diffused into the EC sols. Then the action of solvent volatilization would accelerate the diffusion of uranyl nitrate into the EC sol layer, together with the coordination action of the hydroxyl groups in the EC polymer chains, so the uranyl nitrates would finally be captured and then enter into the EC polymer chains. Besides, with the continuous volatilization of solvent, the solid content increased together with the continuous increase in EC sol viscosity, and the EC polymer chains appeared to be overlapping and entangled in concentrated sol. Moreover, an EC-U

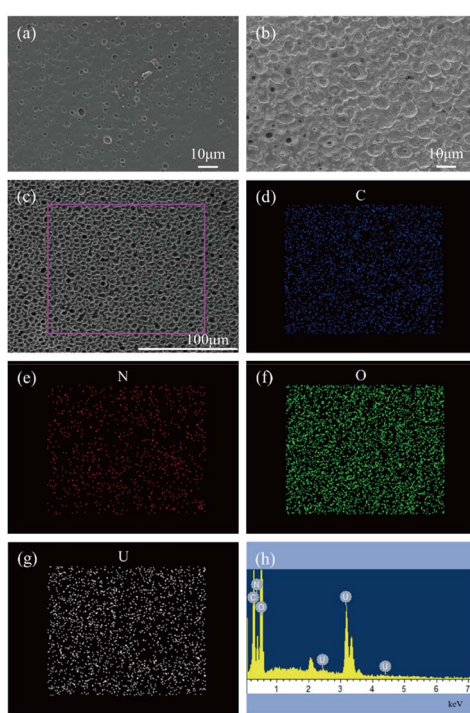


Fig. 8 Characterization. SEM micrographs of EC film before decontamination (a) and after decontamination (b) and (c); mapping images of the selected region of the EC film (d)–(g); EDS of the selected region of the EC film (h).

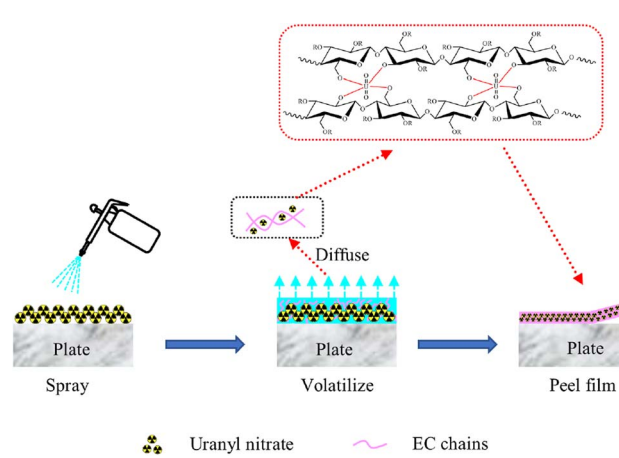


Fig. 10 Schematic diagram of mechanism of decontamination.



complex, centered around the uranyl ion, was formed between multiple EC polymer chains.

As a result, the EC sols gradually accumulated to form a uniform and fine network structure film, with the contaminants being encapsulated gradually and simultaneously fixed in the films.<sup>16</sup> When the films were peeled off, the contaminants would be removed.

In conclusion, the decontamination mechanism of EC sols consisted of at least three actions: diffusion, complexation and embedding.

## 4. Conclusions

In this study, EC sols were prepared with EC being dissolved in green organic solvents of anhydrous ethanol and ethyl acetate. Analysis of rheological behavior disclosed that the EC sols were pseudoplastic fluids and obeyed the Ostwald-de Waele power law, when the temperature ranged from  $-10^{\circ}\text{C}$  to  $0^{\circ}\text{C}$ . Besides, the viscosity of the EC sols decreased as the temperature increased and the EC concentration decreased. Furthermore, the viscosity of the EC sols could be reduced by stirring, which was convenient for large-area spraying during decontamination at a temperature below  $0^{\circ}\text{C}$ . The EC polymer film was formed with the polymer chains of EC being crosslinked and solidified after volatilization of the solvent in the EC sols. Simultaneously, an EC-U complex was formed between multiple EC polymer chains centered around the uranyl ion. At the temperature of  $-10^{\circ}\text{C}$ , the comprehensive decontamination rates on marble, stainless steel, ceramic tile and glass plates were all over 90%, while that on concrete was over 85%. The decontamination mechanism of EC sols consisted of at least three actions: diffusion, complexation and embedding. The EC sols could be the best choice as a basic material for preparing a strippable film detergent in removing radioactive contaminants at low temperatures below  $0^{\circ}\text{C}$ .

## Author contributions

Xunhai Pan: conceptualization, methodology, formal analysis, investigation, data curation, writing – original draft. Xiaoyan Lin: methodology, funding acquisition, writing – review & editing, project administration. Hao Zhang: formal analysis, investigation. Lili Liang: conceptualization, writing – review. Chunxia Pang: conceptualization, formal analysis. Kai Gu: investigation, data curation. Yang Hu: formal analysis, conceptualization. Hailing Xi: formal analysis, investigation, supervision.

## Conflicts of interest

There are no conflicts to declare.

## Acknowledgements

This work is financially supported by Institute of Chemical Defense, Academy of Military Sciences (TC19046DN/5) and Engineering Research Center of Biomass Materials, Ministry of Education, China.

## References

- R. Pravalie and G. Bandoc, *J. Environ. Manage.*, 2018, **209**, 81–92.
- K. Akahane, S. Yonai, S. Fukuda, N. Miyahara, H. Yasuda, K. Iwaoka, M. Matsumoto, A. Fukumura and M. Akashi, *Sci. Rep.*, 2013, **3**, 1670.
- N. A. Beresford, S. Fesenko, A. Konoplev, L. Skuterud, J. T. Smith and G. Voigt, *J. Environ. Radioact.*, 2016, **157**, 77–89.
- S. Kim, B.-I. Min, K. Park, B.-M. Yang, J. Kim and K.-S. Suh, *J. Radioanal. Nucl. Chem.*, 2018, **316**, 1091–1098.
- M. Lopez-Vicente, Y. Onda, J. Takahashi, H. Kato, S. Chayama and K. Hisadome, *Environ. Pollut.*, 2018, **239**, 448–456.
- G. Steinhauser, A. Brandl and T. E. Johnson, *Sci. Total Environ.*, 2014, **470**, 800–817.
- H. Saito, *Poetics*, 2022, **93**, 101594.
- P. Delaporte, M. Gastaud, W. Marine, M. Sentis, O. Uteza, P. Thouvenot, J. L. Alcaraz, J. M. Le Samedy and D. Blin, *Appl. Surf. Sci.*, 2003, **208–209**, 298–305.
- G. Greifzu, T. Kahl, M. Herrmann, W. Lippmann and A. Hurtado, *Opt. Laser Technol.*, 2019, **117**, 293–298.
- M. D. Kaminski, S. D. Lee and M. Magnuson, *J. Hazard. Mater.*, 2016, **305**, 67–86.
- A. Wadood Khan, S. Kotta, S. Hussain Ansari, R. Kumar Sharma, V. Kumar, S. Rana and J. Ali, *J. Renewable Sustainable Energy*, 2012, **4**, 012704.
- J. Wang, G. Q. Liu, L. Zhao, S. H. Wang and J. Li, *J. Radioanal. Nucl. Chem.*, 2019, **322**, 1049–1054.
- H. M. Yang, C. W. Park and K. W. Lee, *J. Hazard. Mater.*, 2019, **362**, 72–81.
- H. Zhang, H. Xi, Z. Li, X. Pan, Y. Wang, C. Chen, X. Lin and X. Luo, *Colloids Surf., A*, 2021, **624**, 126774.
- P. G. Wagle, S. S. Tamboli and A. P. More, *Prog. Org. Coat.*, 2021, **150**, 106005.
- K. Zhang, S. Wang, Z. He, M. Wu and X. Cao, *Appl. Radiat. Isot.*, 2020, **162**, 109187.
- Z. He, Y. Li, Z. Xiao, H. Jiang, Y. Zhou and D. Luo, *Polymers*, 2020, **12**, 1556.
- D. Pulpea, T. Rotariu, G. Toader, G. B. Pulpea, V. Neculae and M. Teodorescu, *Chemosphere*, 2020, **258**, 127227.
- H. M. Yang, C. W. Park and K. W. Lee, *Prog. Nucl. Energy*, 2018, **104**, 67–74.
- H.-M. Yang, K. S. Hwang, C. W. Park and K.-W. Lee, *Ann. Nucl. Energy*, 2017, **109**, 359–364.
- H.-M. Yang, I.-H. Yoon and Y. Lee, *Chem. Eng. J.*, 2020, **402**, 126299.
- X. Xu, X. Pan, J. Li, Z. Li, Y. Xie and X. Lin, *Chemosphere*, 2022, **308**, 136187.
- F. Lu, J. Song, B. W. Cheng, X. J. Ji and L. J. Wang, *Cellulose*, 2013, **20**, 1343–1352.
- P. Filipa and S. Lúcia, *Food Hydrocolloids*, 2018, **84**, 104–116.
- M. Li, J. L. Xia, C. X. Ding, W. Mao, H. Y. Ding, L. N. Xu and S. H. Li, *Carbohydr. Polym.*, 2017, **175**, 131–140.
- A. Zaitoon and L.-T. Lim, *Materialia*, 2020, **10**, 100649.



27 H. Zhang, B. Lin, J. Tang, Y. Wang, H. Wang, H. Zhang, J. Cao, J. Hou, M. Sun and H. Zhang, *Surf. Coat. Technol.*, 2021, **424**, 127647.

28 Y. K. Bai, C. Jiang, Q. H. Wang and T. M. Wang, *Carbohydr. Polym.*, 2013, **96**, 522–527.

29 X. Chen, Y. Zhang, H. Wang, S.-W. Wang, S. Liang and R. H. Colby, *J. Rheol.*, 2011, **55**, 485–494.

30 F. Lu, B. W. Cheng, J. Song and Y. Liang, *J. Appl. Polym. Sci.*, 2012, **124**, 3419–3425.

31 L. J. Wang, G. Lei, B. W. Cheng, X. J. Ji, J. Song and L. Fei, *Carbohydr. Polym.*, 2014, **110**, 292–297.

32 V. K. Vorobiov, M. P. Sokolova, N. V. Bobrova, V. Y. Elokhovsky and M. A. Smirnov, *Carbohydr. Polym.*, 2022, **290**, 119475.

33 R. Masrat, M. Maswal, O. A. Chat, G. M. Rather and A. A. Dar, *Colloids Surf., A*, 2016, **489**, 113–121.

34 M. G. Bekaroglu, Y. Isci and S. Isci, *Mater. Sci. Eng., C*, 2017, **78**, 847–853.

35 K. Inukai, Y. Takahashi, K. Ri and W. Shin, *Ceram. Int.*, 2015, **41**, 5959–5966.

36 C. L. Ang, K. K. Tha Goh, K. Lim and L. Matia-Merino, *Food Hydrocolloids*, 2021, **120**, 106908.

37 V. A. Burmistrov, I. M. Lipatova, J. A. Rodicheva, N. V. Losev, I. P. Trifonova and O. I. Koifman, *Eur. Polym. J.*, 2019, **120**, 109209.

38 Y. Zare, S. P. Park and K. Y. Rhee, *Results Phys.*, 2019, **13**, 102245.

39 P. J. Shi, Y. Zuo, Q. Zou, J. Shen, L. Zhang, Y. B. Li and Y. S. Morsi, *Int. J. Pharm.*, 2009, **375**, 67–74.

40 Y. B. Sun, S. B. Yang, Y. Chen, C. C. Ding, W. C. Cheng and X. K. Wang, *Environ. Sci. Technol.*, 2015, **49**, 4255–4262.

41 J. Yu, X. Luo, B. Liu, J. Zhou, J. Feng, W. Zhu, S. Wang, Y. Zhang, X. Lin and P. Chen, *J. Mater. Chem. A*, 2018, **6**, 15359–15370.

42 S. T. Sikkosana, T. P. Gumede, N. J. Malebo, A. O. Ogundehi and B. Motloung, *Polym. Eng. Sci.*, 2023, **63**, 1411–1422.

43 B. W. Hu, Q. Y. Hu, D. Xu and C. G. Chen, *Sep. Purif. Technol.*, 2017, **175**, 140–146.

44 A. Hivechi, S. H. Bahrami, R. A. Siegel, P. B. Milan and M. Amoupour, *Cellulose*, 2020, **27**, 5179–5196.

45 C. Pang, H. Wang and X. Lin, *Colloids Surf., A*, 2021, **630**, 127643.

